Sato et al. Earth, Planets and Space (2018) 70:163
https://doi.org/10.1186/s40623-018-0934-1

Earth, Planets and Space

FRONTIER LETTER

Open Access

Imaging high-latitude plasma density irregularities resulting from particle precipitation: spaceborne L-band SAR and EISCAT observations

Hiroatsu Sato[1*], Jun Su Kim[2], Norbert Jakowski[1] and Ingemar Häggström[3]

Abstract

High-latitude, small-scale plasma density irregularities are observed by the Advanced Land Observation Satellite 2, Phase Array type L-band Synthetic Aperture Radar-2 and the European Incoherent Scatter radar in Tromsø, Norway. Under high levels of ionization of up to approximately 300 km in height triggered by nighttime particle precipitation, high-resolution SAR images detect horizontal distributions of azimuth shifts resulting from the spatial gradients of electron density. The irregular electron density is characterized by tens of kilometers of band-like structures aligned in the east–west direction with small patch-like structures. We present a method for estimating the local change of TEC gradient and the height of ionospheric irregularities by using single-image SAR sub-band data. The results suggest that these observed structures are likely to be associated with density irregularities caused by precipitating electrons that may have been cascaded into smaller scales by plasma instability processes at F region altitudes. This study presents the first coordinated observations of high-latitude ionosphere features by using SAR satellites and incoherent scatter radar.

Keywords: Ionosphere, High latitudes, TEC, SAR, EISCAT

Introduction

Particle precipitation represents an important source of irregular plasma density structures in the high-latitude ionosphere. Soft electron particles (<1 keV) can spur local increases and decreases in plasma density over more than 10 km. This primary F layer structure can be cascaded into smaller scales through instability processes (Kelley et al. 1982; Tsunoda 1988). E layer density irregularities produced by more energetic particles are likely to be damped faster (Tsunoda 1988). Small-scale F region irregularities of hundreds of meters and of shorter scale sizes can be maintained through turbulent diffusion processes (Kelley et al. 1982).

Such irregular ionospheric electron density structures scatter and diffract electromagnetic radio waves, creating unexpected fluctuations in the received satellite signal through a process known as radio scintillation. At L-band signal frequencies (1–2 GHz) commonly used in radio systems for communication navigation and earth observation, high-latitude scintillations are primarily observed as phase fluctuations caused by plasma irregularities with scale sizes of hundreds of meters to several kilometers (Kintner et al. 2007). The impact of high-latitude and polar ionospheric irregularities is often measured from rapid changes in the total electron content (TEC) level derived from the dual frequency phase measurements of the global positioning system (GPS) and more generally from global navigation satellite system (GNSS) signals (e.g., Aarons 1997; Aarons and Lin 1999; Aarons et al. 2000; Prikryl et al. 2010; Oksavik et al. 2015). The most severe effects such as cycle slips and phase scintillation, which can represent a major operational threat, are

*Correspondence: hiroatsu.sato@dlr.de
[1] Institute of Communication and Navigations, German Aerospace Center, Kalkhorstweg 53, 17235 Neustrelitz, Germany
Full list of author information is available at the end of the article

found to be associated with regions in which sharp TEC gradients are present (e.g., Mitchell et al. 2005; Prikryl et al. 2010). However, the variation in spatial TEC gradients is not fully understood in relation to localized space weather phenomena (e.g., particle precipitation). Small-scale plasma irregularities of tens of kilometers are not well covered by single satellite-receiver ray paths.

Low-frequency synthetic aperture radar (SAR) systems have been suggested to achieve the mapping of small-scale ionospheric TEC distributions at a finer resolution than do GPS/GNSS measurements (Meyer et al. 2006; Pi et al. 2011). Modern spaceborne SAR systems such as L-band ALOS/ALOS-2 deliver meter to sub-meter-scale resolution surface mapping. Spatially varying TEC distributions create phase errors, spurs defocusing in SAR Single-look complex (SLC) data and leads to an azimuth (along satellite track direction) shift of focusing position. The azimuth shift observed in an L-band SAR image is an important measure that can be used to estimate small-scale ionospheric density irregularities and associated spatial variations in TEC. SAR images containing streak-like structures known as azimuth streaks were first reported through C-band SAR (5.3 GHz) interferometry of a polar region (Gray et al. 2000). L-band SAR (1.2 GHz) is more sensitive to TEC gradients. The effects of the small-scale structures in the ionosphere on the SAR images can be further analyzed by applying SAR image processing techniques, especially when simultaneous observations of plasma density information are available (Kim et al. 2016). In cases involving plasma irregularities of up to tens of kilometers in scale (commonly observed during magnetic storms at high latitudes), L-band SAR is expected to detect them in the form of rapid changes in azimuth shift estimates.

The objective of this article is to present a coordinated observation of the horizontal distributions of TEC of the high-latitude ionosphere from L-band SAR and incoherent scatter radar. Enhancements in electron density and temperature values are observed over a wide range of altitudes by the EISCAT ultra-high-frequency (UHF) radar near Tromsø, Norway. Local changes of TEC gradients are mapped at a fine scale by means of the sub-band azimuth shift from single SAR images acquired via the ALOS-2 PALSAR-2. We estimate the height of ionospheric disturbances that have impacted SAR signals.

SAR azimuth shifts and TEC gradients

To characterize ionospheric density irregularities, we estimate the spatial distribution of TEC gradients drawn from the azimuth direction shift between sub-band SAR images. The azimuth direction refers to the direction parallel to the direction of satellite motion. The azimuth direction focusing of SAR utilizes frequency modulation generated by a change in the relative positioning of antenna with respect to the scatterer as the antenna proceeds. The Doppler frequency changes from positive to negative during the synthetic aperture (Curlander and McDonough 1991), as illustrated in Fig. 1. For most spaceborne SAR sensors orbiting sun-synchronously, this procedure is completed within a few seconds and within a narrow beam width of a few degrees. The lengths of the synthetic apertures of current spaceborne SAR systems are approximately 10–20 km.

The gradient of TEC in the azimuth direction modulates the ideal time-Doppler relationships of SAR signals, leading to a shift in the focusing position (Gray et al. 2000; Wegmüller et al. 2006; Kim et al. 2015, 2016). The shift in azimuth focus Δa and the TEC gradient are related by

$$\Delta a = \frac{\zeta r_0}{f_0^2 \cos\beta} \frac{h_{\mathrm{iono}}}{h_{\mathrm{sat}}} \frac{\partial N_{TEC}}{\partial x}, \tag{1}$$

where $\zeta = 40.31\ \mathrm{m^3/s^2}$, r_0 is the shortest distance from the antenna to the scatterer, f_0 is the center frequency, β is the angle between the antenna and the scatterer measured at the center of the Earth, h_{iono} and h_{sat} are the assumed heights of the ionosphere and of the satellite mounting of the antenna, and $\partial N_{TEC}/\partial x$ is the gradient of TEC in the azimuth direction. In the case of the ALOS-2 PALSAR-2 system used in this study, 1 m of azimuth shift is induced by a TEC gradient of 1 TECU/100 km (1 TECU corresponds to 10^{16} electrons/m^2) for the ionospheric piercing point at the altitude of $h_{\mathrm{iono}} = h_{\mathrm{sat}}/2$. Therefore, small-scale TEC gradients are detectable from ALOS-2 PALSAR-2, which has a meter-scale resolution in the azimuth direction.

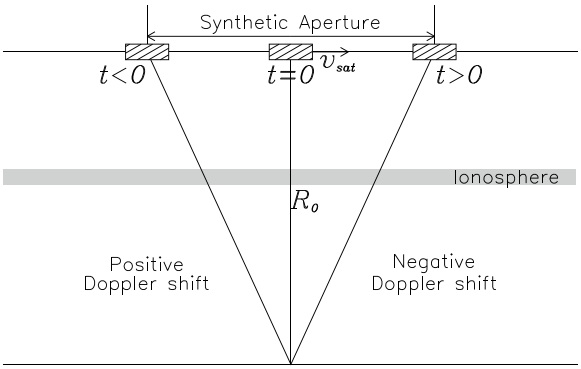

Fig. 1 Geometric configuration of azimuth direction SAR imaging through the ionosphere. The progression of the antenna over the synthetic aperture period, corresponding changes in direction and Doppler shifts are shown

The estimation of the azimuth shift in an SAR image involves the comparison of two SAR images. A SAR image of interest can be compared with another SAR image of similar geometry acquired at a different time as in (Gray et al. 2000). This approach reveals relative azimuth shifts between two images that represent the difference in TEC gradients observed at two acquisition times if there is no ground motion during the acquisition interval. This approach generates intrinsically ambiguous results: only the difference in the two TEC gradients is detected, and each absolute TEC gradient is lost.

The azimuth shift can also be acquired between azimuth sub-band images. From a part of the full azimuth spectra of an SAR image, it is possible to generate a SAR image of the same spatial extent at the cost of reducing the resolution, i.e., increasing the spatial separation of independent samples. It is possible to compare any two sub-band images to estimate the azimuth shift occurring between them. As the azimuth focusing of SAR relies on the Doppler Effect related to the motion of an antenna, the position of an antenna and the Doppler frequency of the azimuth sub-band are linearly related. The azimuth shift estimated between two sub-band images represents the difference in TEC gradients observed at separate positions (see Fig. 1.). In this study, this measure is named as local change of TEC gradients and we used azimuth sub-band shift as its proxy. Assuming the occurrence of slow enough TEC variations during the synthetic aperture period (2.27 s for the investigated SAR observations), the sub-band azimuth shift represents the absolute value of the second-order derivative of the TEC of the azimuth direction.

Observations

Experimental setup

The EISCAT UHF radar system (Rishbeth and van Eyken 1993) located near Tromsø, Norway (69.58°N, 19.21°E) is an incoherent scatter radar system with functioning at an operation frequency of 930 MHz. The 32 m parabolic dish of the UHF radar antenna is steerable in both the azimuth and elevation directions. UHF radar data used in this study were analyzed using Grand Unified Incoherent Scatter Design and Analysis Package (GUISDAP) software (Lehtinen and Huuskonen 1996) to obtain the altitude profile of electron density and temperature. We applied a time resolution of 1 min, except when the dish was swinging to observe satellite directions.

On February 9, 2017, the UHF radar system was operated under the EISCAT peer review program for coordinated observation with the ALOS-2 satellite. The EISCAT radar beam was directed field-aligned from 18:00 to 21:49 UT. The field-aligned direction of the radar was set to an elevation/azimuth angle of 77.6°/187.0°. The UHF radar system was then operated in the satellite following mode, and the radar dish swung from 21:50 UT (41.8°/194.3°) until 21:54 UT (32.1°/322.6°). The radar direction was fixed from 21:54 UT until 22:00 UT.

The SAR images used in this study were acquired from ALOS-2 PALSAR-2 operated by the Japan Aerospace Exploration Agency (JAXA). ALOS-2 orbits at approximately 628 km in altitude at an inclination angle of 97.9° in a sun-synchronous orbit. The PALSAR-2 instrument operates at different center frequencies of 1236.5, 1257.5 and 1278.5 MHz depending on the imaging modes with equivalent wavelengths of 24.2, 23.8, and 23.4 cm, respectively.

Figure 2 illustrates the SAR imaging geometry observed over the Tromsø area on February 9, 2017. The ALOS-2 satellite followed an ascending orbit oriented south to north. Satellite flight direction (azimuth direction) and radar look direction are denoted by black arrows. Red rectangles highlight the observation area at image center times 21:51:28 UT and 21:51:36 UT corresponding to ALOS-2 scene ID's ALOS2146791400 and ALOS2146791410, respectively. For these images, the observation mode is set to SM3 (Stripmap3), and the

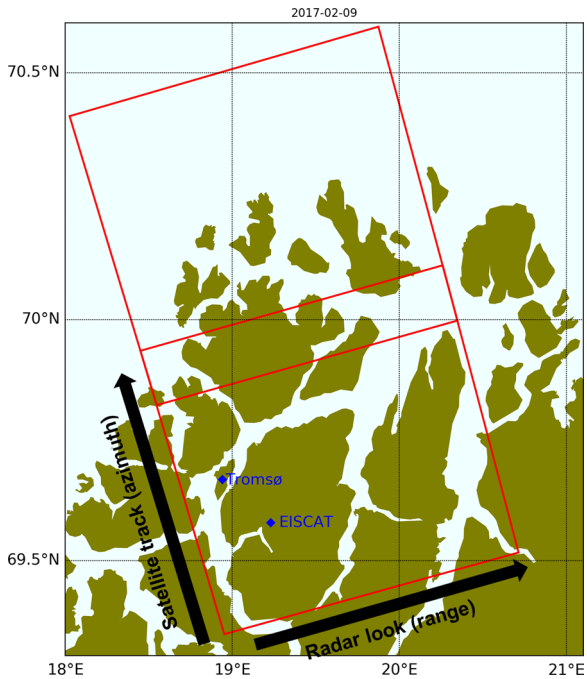

Fig. 2 ALOS-2/PALSAR-2 SAR image acquisition geometry measured on February 9, 2017. ALOS-2 was ascended from south to north with right-oriented geometry denoted by black arrows. The lower and upper red rectangles correspond to SAR images with the center times of 21:51:28 UT and 21:51:36 UT (ID Numbers ALOS2146791400 and ALOS2146791410). The locations of EISCAT radar systems are marked with blue diamonds

image width is 70 km with a pixel spacing of 9.1 m in range and 3.5 m in azimuth.

EISCAT electron density and temperature profiles

Figure 3 shows the electron density (Ne) and electron temperature (Te) values as a function of altitude and time derived from the EISCAT UHF measurements collected from 21:05 to 22:00 UT on February 9, 2017. A data resolution of 1 min was used when the radar system was fixed in direction. The radar swinging geometry and limited integration time create uncertainty in the UHF data, especially for the high altitudes observed at 21:50 UT and 21:51 UT. Accordingly, a gap in the data is observed for this time interval (the white area) until the radar direction is fixed at 21:54 UT onward in the northwest direction. Although this data limitation prevents us from making exact simultaneous observations from SAR and EISCAT, Fig. 3 shows that the electron densities observed in the F and E regions were continually enhanced throughout the experiment, and we infer that no significant deviations from this trend could be observed at the data gap interval. When density enhancement occurs at 100 km to 300 km in altitude (e.g., 21:08 to 21:15 UT), the electron temperature significantly increases in the F region positioned above 200 km, showing that both effects can be attributed to the energy generated through the simultaneous precipitation of soft (< 1 keV) and hard (< 100 keV) particles. The occurrence of electron heating here is attributed to primary ionization occurring due to the precipitation of energetic particles and the production of secondary electrons, which lose their energy through collisions with ambient electrons (Walker and Rees 1968). Similar synchronizations of density increase, and F region temperature enhancements have been observed from EISCAT UHF radar data (Oyama et al. 2014), distinguishing the origins of ionization from other sources (e.g., convection from the dayside not accompanied by temperature enhancement).

Figure 3 also shows that the energy spectrum of precipitating electrons is not uniform for the observation period. Low electron densities at heights of between 150 km and 200 km are occasionally found (e.g., at 21:39 to 21:45 UT). This separated E and F regions of electron density profiles can likely be attributed to a change in the energy spectrum of precipitation, as noted for previous observations (Oyama et al. 2014). A notable decline in density occurred from 21:46UT and 21:49 UT within the F layer at between 260 and 300 km in altitude. Despite data limitations, Fig. 3 indicate that particle fluxes enhancing ionization within this altitude range were refilled over the next few minutes or at least before the radar system became fixed at 21:54 UT.

SAR azimuth shifts observed in sub-band images

Figure 4 shows a color-coded SAR sub-band azimuth shift in meters derived from SLC data at 21:51:28 UT

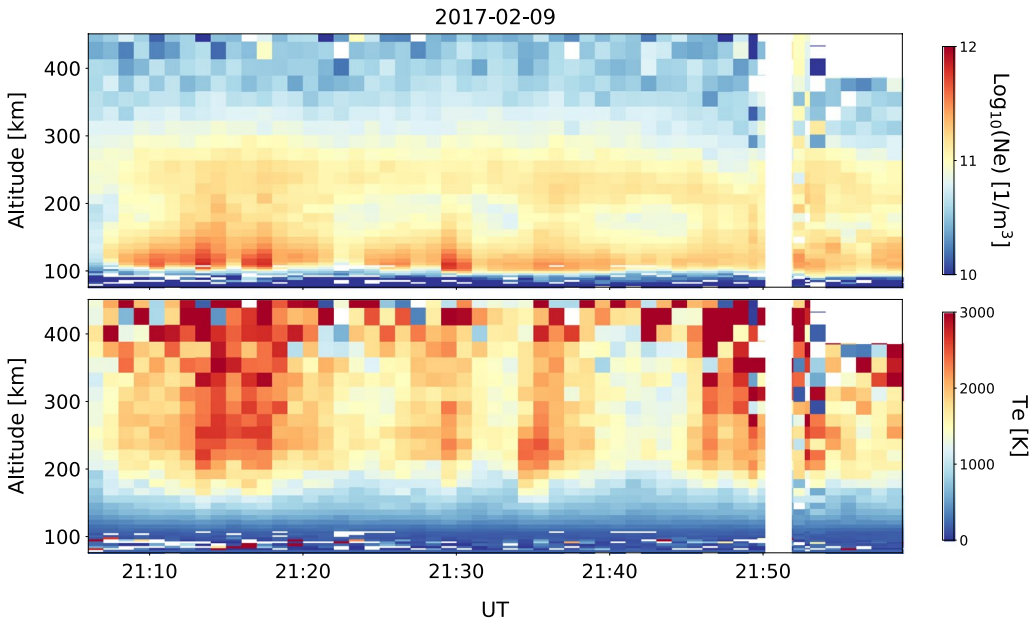

Fig. 3 EISCAT UHF radar observations collected on February 9, 2017. Electron density (top) and electron temperature (bottom) values are color-coded as a function of time and altitude. The UHF radar system is oriented in the field-aligned direction from the start of the experiment until 21:49 UT. The radar system is swinging from 21:50 to 21:53 UT and is fixed at the lower elevation angle at 21:54 UT

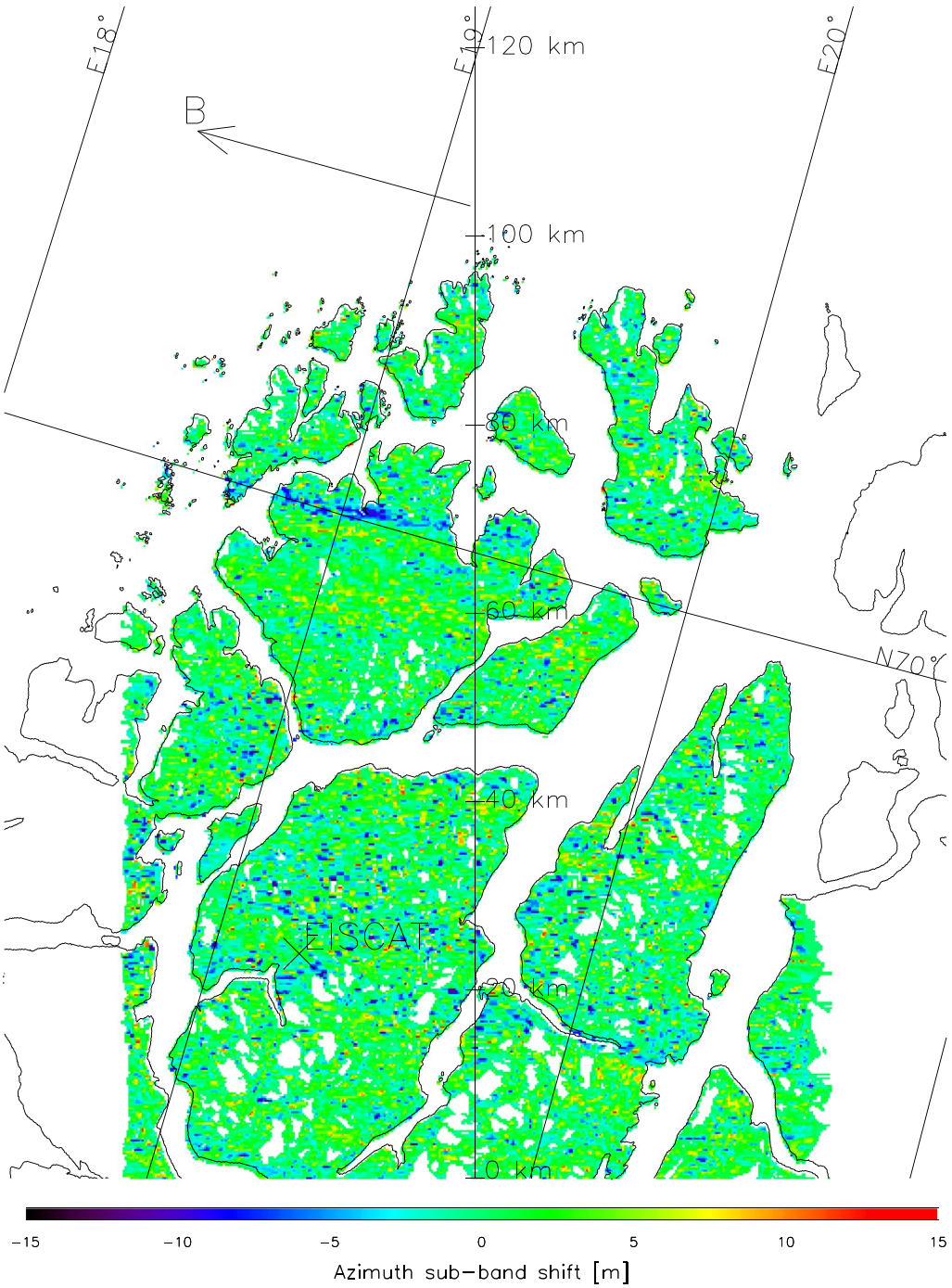

Fig. 4 SAR sub-band azimuth shift derived from raw ALOS-2 SAR data for February 9, 2017. The image is shown with SAR acquisition data collected at 21:51:28 UT and 21:51:36 UT shown in Fig. 2. White areas denote gaps in data resulting from scattering and water masks. Positive (blue) and negative (red) azimuth shifts are distributed as patches of under 1 km. For ionospheric piercing observed at half the satellite altitude, a 1-m sub-band azimuth shift corresponds to a 1 [mTECU/km] TEC gradient. Positive shifts forming a larger east–west structure are observed at the 70-degree latitude line. The green area shows gradual changes in background TEC

and 21:51:36 UT. Azimuth sub-band shifts are estimated from the amplitude cross-correlation of sub-band SAR images. The estimation is performed for each 530 m (range) by 310 m (azimuth) rectangle, which corresponds to 64 by 32 samples of sub-band images. The white areas denote gaps in the azimuth shift estimation due to the

poor azimuth shift estimates and bad imaging geometry. Scattering over water is also masked out as the relative shift estimation over unstable water surface fails in general. Azimuth shifts shown in the green area are less than a few meters and can be interpreted as the background ionosphere with smooth variations of a few tens of milli-TECU (mTECU) per 1 km gradient at the ionospheric piecing point height. Blue and red areas represent negative and positive azimuth shifts of greater than 5 meters that correspond to local change of TEC gradients more than 50 mTECU per 1 km based on an ionospheric height of half of the orbit altitude.

The estimated SAR azimuths shift due to TEC gradient changes having different scales and structures over the Tromsø area. North of Tromsø at around the 70°N latitude line the negative (blue) azimuth shift forms a clear band-like structure of approximately 30 km in the east–west direction. The band structure stretches to widths of between 4 and 8 km in a north–south direction. With the SAR image data, it is possible to monitor two-dimensional distribution of these density irregularities (almost fully aligned with the east–west component of the magnetic field projected on the SAR images in the present example, as illustrated by the black arrow). At just below the 70°N line, a thinner and patchier positive azimuth shift band is found. More small patch-like structures are found in the southern direction, and both positive and negative azimuth shifts appear to be less closely aligned with the magnetic field direction.

These patches vary in size from kilometer to sub-kilometer scales. We must note that density irregularities shown in the sub- kilometer range in Fig. 4 must be interpreted carefully, as azimuth estimates are performed in the 530 m × 310 m window, and therefore, we cannot eliminate the possibility that any single isolated patches of less than the estimation window size were affected by errors during estimation. Nevertheless, the coexistence of different scale irregularities is evident from Fig. 4, and the small patches may represent segments of a larger structure that cascaded into lower density structures. At this scale, positive and negative azimuth shifts alternate more frequently, which corresponds to more rapid variation in local change of TEC gradients.

Discussion

We have illustrated the spatial distribution of TEC gradient changes from L-band SAR images, while the EISCAT UHF radar data show enhanced levels of electron density due to the presence of precipitating particles. To the best of our knowledge, this study may be the first to make coordinated observations of SAR and altitude profiles of local electron density. Although our EISCAT data present data gaps for the SAR image acquisition period due to the tracking geometry of the fast moving ALOS-2 satellite, our data show that the formation of observed irregularities is triggered by precipitating particles.

SAR observations of ionospheric disturbances are in many cases attributed to F region phenomena (Pi et al. 2011). The high ionization profile up to 300 km shown in Fig. 2 indicates that propagation effects originate primarily from the F region, although potential contributions from highly ionized E regions cannot be ruled out. Recent SAR interferogram studies have shown that discrete E region ionization occurring at midlatitudes can be imaged by SAR phase signals (Maeda et al. 2016; Furuya et al. 2017). From our observations on February 9, 2017, the EISCAT data show continuous enhancements from regions E to F; density enhancements occurring in region E are not significantly discrete.

Here, our goal is to estimate the ionospheric height that essentially contributes to phase changes measured by SAR signals denoted by the azimuth shift. The height estimation technique exploits the parallax observed during the synthetic aperture process. The SAR system scans a scatterer based on a varying geometry that introduces linear Doppler frequency changes. The positive and negative Doppler frequency bands correspond to the geometry within which the antenna is positioned behind and ahead of the scatterer. By measuring the spatial difference in ionospheric features that induces the azimuth shift observed in the two sub-band images, the ionospheric height can be estimated from the simple geometry.

To estimate the ionospheric height from azimuth sub-band shifts, the azimuth bandwidth W is divided into three parts (Fig. 5) (Kim et al. 2016). The first sub-band $-\frac{W}{2} < f < -\frac{W}{6}$ represents the departing geometry, and the last sub-band $\frac{W}{6} < f < \frac{W}{2}$ represents the approaching one. The middle sub-band is centered around the zero-Doppler frequency. An azimuth shift estimation of the first and middle sub-band images yields the azimuth sub-band shift estimated from the departing geometry at $f = -\frac{W}{6}$, while that between the middle and last sub-band does so at $f = \frac{W}{6}$. The two azimuth sub-band shift estimates should be identical, with the exception of their relative offsets in the azimuth direction due to the parallax when the ionosphere does not evolve during the synthetic aperture time. This relative offset is proportional

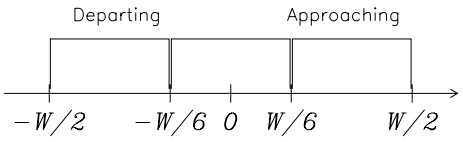

Fig. 5 The separation of the azimuth spectrum for the estimation of the ionospheric altitude. The azimuth bandwidth W is divided into three parts

to the ionospheric height or to the height of ionospheric features responsible for azimuth shifts between azimuth sub-band images. In this configuration, the baseline of the parallax is only a third of the full synthetic aperture length ($= \frac{L_{SA}}{3}$). The relative offset of the two azimuth sub-band shifts L_{offset} and the ionospheric height are related by $\frac{L_{SA}}{3} : L_{\text{offset}} = h_{\text{sat}} : h_{\text{iono}}$.

For ALOS-2 acquisition over the Tromsø area on February 9, 2017, the offset between the azimuth shift estimate L_{offset} is 2.5 km. The synthetic aperture of ALOS-2 is approximately 17 km, and $\frac{L_{SA}}{3}$ is 5.7 km. For a satellite orbit altitude of 641 km at this latitude, the ionospheric piercing point altitude is estimated at 280 km. Therefore, we interpret the observed SAR azimuth shift in the high-latitude ionosphere to be primarily associated with the presence of F region density irregularities. In fact, EISCAT UHF radar data show an intriguing change in density at this altitude immediately prior to the SAR observation period. Electron density enhancements observed at altitudes of 260–300 km are notably lowered, showing that recombination processes temporally dominated at this altitude. At 21:49 UT, the electron density observed within this altitude range reaches a minimum of approximately 283 km, representing the most similar EISCAT density observation made along the field line prior to the SAR observation period. Density irregularities observed via the SAR system may have been associated with subsequent changes in precipitating particle energy that re-ionized the upper F layer.

The SAR observations show a coexistence of small- and large-scale TEC gradients under particle precipitation. In situ rocket measurements collected during auroral particle precipitation in the F region cusp ionosphere show that decameter-scale density structures are located at km-scale density gradients in which gradient drift instability can be effectively excited (Moen et al. 2012; Oksavik et al. 2012).

Figure 4 shows that the TEC gradient changes even below the kilometer scale, at which smaller density structures can form.

Furthermore, as the synthetic aperture period is less than 10 s, the spaceborne SAR may be able capture an irregular electron density distribution triggered by gradient drift instability, for which the characteristic growth time is observed as 40–50 s. While the original ALOS2 SAR image achieves less than a 10-m resolution, this fine resolution is lost when employing the single SAR sub-band technique used in this study to estimate the local change of TEC gradients and its horizontal variations. This limitation may be overcome through future studies that use SAR interferometry to map differential TEC at sub-kilometer-scale resolutions, provided that the ionosphere-induced phase is isolated from other contributions such as troposphere and ground deformation. Through full-polarimetric acquisition, the estimation of absolute TEC is made possible by measuring the Faraday rotation proportional to the TEC value. In this case, TEC can be obtained at kilometer level resolutions (Meyer 2006; Pi et al. 2011).

Conclusions

In this study, we have presented a high-resolution spatial distribution of the local change TEC gradients associated with particle precipitation in the high-latitude ionosphere. L-band SAR image acquisition by ALOS-2 undergoes a significant azimuth shift due to the presence of TEC gradients at spatial scales of kilometers to tens of kilometers when the EISCAT UHF radar measures ionization levels of up to approximately 300 km in altitude, which are triggered by precipitating electrons of varying energy levels. The observed sharp changes in the TEC gradient form east–west aligned bands covering a few tens of kilometers and patch-like structures at or below the kilometer scale. These results suggest that the observed structures are likely associated with original density irregularities caused by precipitation electrons cascading into smaller scales through plasma instability processes at F region heights. We presented the first coordinated observations of the high-latitude ionosphere using SAR and incoherent scatter radar systems. As a result, the data presented here serve as an example of spaceborne SAR imaging and of small-scale horizontal variations in ionospheric electron density. Thus, SAR imaging can be used as a promising tool for exploring small-scale irregularities in the ionosphere and their impacts on other radio systems such as the GNSS.

Abbreviations

SAR: synthetic aperture radar; ALOS-2: advanced land observation satellite 2; EISCAT: European Incoherent Scatter Scientific Association; GNSS: global navigation satellite system; GPS: global positioning system; GUISDAP: grand unified incoherent scatter design and analysis package; JAXA: Japan Aerospace Exploration Agency; PALSAR: phased array L-band synthetic aperture radar; TEC: total electron content; UHF: ultra-high frequency.

Authors' contributions

HS and JSK led the experiment and SAR data analysis and wrote the manuscript. NJ contributed to the research plan and to the manuscript. IH processed and analyzed the EISCAT data. All authors read and approved the final manuscript.

Author details

[1] Institute of Communication and Navigations, German Aerospace Center, Kalkhorstweg 53, 17235 Neustrelitz, Germany. [2] Microwaves and Radar Institute, German Aerospace Center, 82234 Wessling, Germany. [3] EISCAT Scientific Association, Kiruna, Sweden.

Acknowledgements

The experiment was supported by the EISCAT peer-reviewed program. EISCAT is an international association supported by research organizations operating in China (CRIRP), Finland (SA), Japan (NIPR and STEL), Norway (NFR), Sweden

(VR) and the United Kingdom (NERC). ALOS-2 PALSAR-2 data are provided by the Japan Aerospace Exploration Agency (JAXA).

Competing interests
The authors declare that they have no competing interests.

Availability of data and materials
The EISCAT data are available from the Madrigal database (https://www.eiscat.se/madrigal/). ALOS-2/PALSAR-2 data can be obtained from the AUIG2 archive data search Web site (https://auig2.jaxa.jp/openam/UI/Login).

Consent for publication
Not applicable.

Ethics approval and consent to participate
Not applicable.

Funding
Not applicable.

Publisher's Note

Received: 2 March 2018 Accepted: 26 September 2018
Published online: 04 October 2018

References

Curlander JC, McDonough RN (1991) Synthetic aperture radar: system and signal processing. Wiley, London

Furuya M, Suzuki T, Maeda J, Heki K (2017) Midlatitude sporadic-E episodes viewed by L-band split-spectrum InSAR. Earth Planets Space 69:175. https://doi.org/10.1186/s40623-017-0764-6

Gray AL, Mattar KE, Sofko G (2000) Influence of ionospheric electron density fluctuations on satellite radar interferometry. Geophys Res Lett 27:1451–1454. https://doi.org/10.1029/2000gl000016

Kelley MC, Vickrey JF, Carlson CW, Torbert R (1982) On the origin and spatial extent of high-latitude F region irregularities. J Geophys Res Sp Phys 87:4469–4475. https://doi.org/10.1029/JA087iA06p04469

Kim JS, Papathanassiou K, Scheiber R, Quegan S (2015) Correcting distortion of polarimetric SAR data induced by ionospheric scintillation. IEEE Trans Geosci Remote Sens 53:6319–6335. https://doi.org/10.1109/TGRS.2015.2431856

Kim JS, Sato H, Papathanassiou K (2016) Validation of ionospheric mapping by means of SAR through ground based radar measurements. In: Proceedings of EUSAR 2016. Hamburg, Germany, pp 1090–1095

Kintner PM, Ledvina BM, de Paula ER (2007) GPS and ionospheric scintillations. Sp Weather 5:S09003. https://doi.org/10.1029/2006SW000260

Lehtinen MS, Huuskonen A (1996) General incoherent scatter analysis and GUISDAP. J Atmos Terr Phys 58:435–452. https://doi.org/10.1016/0021-9169(95)00047-X

Maeda J, Suzuki T, Furuya M, Heki K (2016) Imaging the midlatitude sporadic E plasma patches with a coordinated observation of spaceborne InSAR and GPS total electron content. Geophys Res Lett 43:1419–1425. https://doi.org/10.1002/2015GL067585

Meyer F, Bamler R, Jakowski N, Fritz T (2006) The potential of low-frequency SAR systems for mapping ionospheric TEC distributions. IEEE Geosci Remote Sens Lett 3:560–564. https://doi.org/10.1109/LGRS.2006.882148

Mitchell CN, Alfonsi L, De Franceschi G et al (2005) GPS TEC and scintillation measurements from the polar ionosphere during the October 2003 storm. Geophys Res Lett 32:12S03. https://doi.org/10.1029/2004GL021644

Moen J, Oksavik K, Abe T et al (2012) First in situ measurements of HF radar echoing targets. Geophys Res Lett 39:L07104. https://doi.org/10.1029/2012GL051407

Oksavik K, Moen J, Lester M et al (2012) In situ measurements of plasma irregularity growth in the cusp ionosphere. J Geophys Res Sp Phys 117:A11301. https://doi.org/10.1029/2012JA017835

Oyama S, Miyoshi Y, Shiokawa K et al (2014) Height-dependent ionospheric variations in the vicinity of nightside poleward expanding aurora after substorm onset. J Geophys Res Sp Phys 119:4146–4156. https://doi.org/10.1002/2013JA019704

Pi X, Freeman A, Chapman B et al (2011) Imaging ionospheric inhomogeneities using spaceborne synthetic aperture radar. J Geophys Res Sp Phys. https://doi.org/10.1029/2010JA016267

Prikryl P, Jayachandran PT, Mushini SC et al (2010) GPS TEC, scintillation and cycle slips observed at high latitudes during solar minimum. Ann Geophys. https://doi.org/10.5194/angeo-28-1307-2010

Rishbeth H, van Eyken AP (1993) EISCAT: early history and the first ten years of operation. J Atmos Terr Phys 55:525–542. https://doi.org/10.1016/0021-9169(93)90002-G

Tsunoda RT (1988) High-latitude F region irregularities: a review and synthesis. Rev Geophys 26:719–760

Walker JCG, Rees MH (1968) Ionospheric electron densities and temperatures in aurora. Planet Space Sci 16:459–475. https://doi.org/10.1016/0032-0633(68)90161-X

Wegmüller U, Werner C, Strozzi T, WiesmannA (2006) Ionospheric electron concentration effects on SAR and InSAR. In: Proceedings of IGARSS2006. Denver, USA